Check for updates

Controllable fabrication of single-crystalline, ultrafine and high-silica hierarchical ZSM-5 aggregates *via* solid-like state conversion†

Hongyao Li,* Yaquan Wang, [ID] Fanjun Meng, Fei Gao, Chao Sun, Chunyang Fan, Xiao Wang and Shuhai Wang

A series of single-crystalline, superfine and high-silica ($SiO_2/Al_2O_3 > 100$) hierarchical ZSM-5 aggregates (denoted as HA-ZSM-5) with a tuneable crystal morphology and size, and rich intercrystalline mesoporosity, were facilely fabricated within a short reaction time using the commercially available *n*-hexyltrimethylammonium bromide (HTAB) as a mesopore template by a solid-like state conversion (SSC) route; the crystallization of HA-ZSM-5 is induced within 36 h at a $HTAB/SiO_2$ ratio of 0.05 with the assistance of 2% silicalite 1 (S-1) seeds. Key factors (such as SiO_2/Al_2O_3 ratio, seed/SiO_2 ratio and HTAB/SiO_2 ratio) in controlling the crystal size and morphology have been systematically investigated. The formation process was studied by monitoring the morphology, relative crystallinity and structural properties of the samples at different crystallization times. The preparation of HA-ZSM-5 zeolites may be a kinetics-controlled dissolution/induction/growth/aggregation process and the possible formation mechanism was put forward based on experimental results. The obtained samples were characterized by several techniques and the representative HA-ZSM-5 (HA-167-2S-5H) was evaluated in a methanol to propylene (MTP) reaction. Compared with the blank sample (denoted as C-ZSM-5) without HTAB addition and a commercial ZSM-5 zeolite (denoted as C_1-ZSM-5), the HA-167-2S-5H sample exhibited the highest selectivity towards propylene (40.1% *vs.* 33.1% and 38.7%) and butylene (22.9% *vs.* 17.2% and 21.4%), and especially the longest catalytic lifetime (22 h *vs.* 6 h and 1.5 h). The remarkably enhanced catalytic performance of HA-167-2S-5H could be attributed to the synergistic effect of the excellent structural properties, appropriate acidity and good accessibility of acidic sites. In addition, the introduction of interparticle mesopores not only enhances the utilization of zeolite acid sites by the enlarged external surface but also partially suppresses side reactions and inhibits coke deposition by shortening the micropore diffusion path lengths, leading to an increased conversion.

1. Introduction

ZSM-5 zeolites, with MFI-type topology, have been extensively applied as industrial catalysts for various petrochemical processes owing to their variable acidity, good shape selectivity and strong hydrothermal stability.[1] But the relatively narrow individual micropores of conventional ZSM-5 zeolites often impose diffusion limitations that severely hinder their further applications in bulky-molecule-involved process.[2] To address this intractable issue, two main synthetic strategies have been proposed to reduce the diffusion resistance of large molecules in recent years.[3] Decreasing the size of zeolite in nanoscale to shorten the inner diffusion path length of bulky substrates

becomes a natural choice.[4] Nonetheless, the low yield in preparation, low thermal stability and difficult separation of superfine nanocrystals from the reaction mixture limit their practical application.[5] Another efficient option for solving the above mentioned diffusion limitations is to construct hierarchically structured zeolites (HSZs), coupling a microporous crystalline framework with auxiliary mesoporous structure, which is considered to be an effective approach stimulating wide research.[6] For instance, both hard templates, such as carbon nanotubes,[7] activated carbon,[8] carbon nanofibers[9] and soft templates, such as polymers[10] and surfactants[11,12] have been employed as mesoporogens in the synthesis of HSZs. Combined with the high cost, energy-intensive and troublesome pre-preparation of hard templates, soft templating method seems a more promising candidate for synthesising HSZs owing to its inherent advantages of easily tunable mesopores and good compatibility with the synthesis solution.[13] As a very successful example of HSZs, hierarchical ZSM-5 aggregates (denoted as HA-ZSM-5) combine dual advantages of both nanosized zeolites

Key Laboratory for Green Chemical Technology of the Ministry of Education, School of Chemical Engineering & Technology, Tianjin University, Tianjin 300072, P. R. China. E-mail: lhy0501@163.com; Tel: +86-22-23507881

† Electronic supplementary information (ESI) available: Details of sample characterization and results. See DOI: 10.1039/c7ra03962j
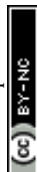
and HSZs, such as a shorter diffusion path length, a larger external surface area and more accessible active sites exhibited in contrast to conventional ZSM-5, while being able to avoid high-speed centrifugation due to their larger secondary particle size.[14] Therefore, HA-ZSM-5 have aroused great interest for their excellent performances and many successful examples of using seeds or soft templates to synthesize HA-ZSM-5 have been reported. It has been reported that silicalite 1 (S-1) seeds have been used to fabricate HA-ZSM-5, however, the obtained HA-ZSM-5 sample remained still in micron range.[15] Meng and co-workers also reported the successful preparation of HA-ZSM-5 by a seed-induced method with S-1 crystals as the seeds, but only the samples with SiO_2/Al_2O_3 ratio of 50 were reported.[16] More importantly, Ryoo *et al.* pioneered the use of a new kind of "two-in-one" template, combining features of both a primary template and a mesogenous template within one molecule, and successfully fabricated ZSM-5 nanosheets aggregates with intracrystal mesopores.[17] Nevertheless, the synthesis process of this bifunctional template involves complex manipulations and the synthesis of ZSM-5 nanosheets stacks becomes costly.[18] Most recently, Chen *et al.*[19] prepared HA-ZSM-5 by seed-inducing *via* a hydrothermal synthesis method in the presence of a long alkyl-chained surfactant (LACS) named cetyl-trimethylammonium bromide (CTAB), whereas CTAB often lead to the occurrence of phase separation between meso- and micro-phases due to the competition between self-assembly and zeolite crystallization.[20] Another drawback of using LACSs in the synthesis of HA-ZSM-5 lies in their poor thermal stability, which may be decompose at high crystallization temperatures.[21] Different from LACSs, short alkyl-chained surfactants (SACSs), such as *n*-hexyltrimethylammonium bromide (HTAB), have strong coulombic interactions toward the zeolite crystals and good thermal stability under high temperature and high pressure conditions.[22] These interactions with nanocrystals may hinder their excessive growth and the stacking of the resulting nano-sized zeolites will form HA-ZSM-5.[23] From an economic and synthetic perspective, it prompted us to try using SACSs to synthesize high silica HA-ZSM-5 with controllable morphologies.

In fact, the above-mentioned synthesis routes also have few inevitable shortcomings, such as procedural complexity (time-consumption), economic feasibility (low yield and high cost) and environmental issues (generating a large amount of waste solvents).[24] Compared with these direct hydrothermal approaches, steam-assisted crystallization (SAC) method is an alternative but more favorable choice. SAC has opened up new possibilities for the synthesis of HA-ZSM-5 and gained more and more attention recently due to its high zeolite yield, few amounts of wastes and low template consumption.[25] Huge efforts have been devoted to synthesize HA-ZSM-5 *via* SAC method. He[26] and Zhang[27] synthesized HA-ZSM-5 *via* SAC method. More recently, Deng *et al.*[28] obtained HA-ZSM-5 *via* glycerol-mediated crystallization using a mesoporous steam-treated dry gel as the precursor. However, industrial applications of SAC method are still limited by the complex manipulations of dry gel preparation because the procedure of vaporizing the solvents are necessary for the preparation of

homogeneous gels.[29] Recently, we synthesized high-silica HA-ZSM-5 ($SiO_2/Al_2O_3 \geq 100$) *via* a SAC method with the aid of a trace of TPAOH.[30]

Fortunately, solid-like state conversion (SSC) method has attracted considerable attention in past years,[31] as it can not only avoid these extra steps of SAC method, but also reserve the advantages of SAC method, such as shortening the crystallization time obviously, improving the yield of the products, and reducing the emission of waste liquids, *etc.* In addition, recent progress has demonstrated that a small amount of water is necessary for the preparation of HA-ZSM-5 in the solid transformation of the dry gel.[24]

As compared with our previous works and based on the ideas of SACSs and SSC method, this present work aimed to make the synthetic process of SAC simplified and this paper reported that single-crystalline, ultrafine and high-silica HA-ZSM-5 were directly synthesized *via* SSC method using commercially available HTAB as the mesoporogen through S-1 seed-induced route. Different from the previous studies, where LACSs were used as templates, our research shows that the SACSs and SSC method are also very effective in the synthesis of high-silica HA-ZSM-5. For comparison, the blank sample (denoted as C-ZSM-5) was synthesized without HTAB addition by a similar procedure. Herein, a very efficient method is developed for the preparation of single-crystalline, ultrafine and high-silica HA-ZSM-5 zeolites. Benefiting from the synergistic effect between HTAB and SSC method, seed/SiO_2 molar ratio is greatly reduced to 0.02, and interesting smaller nanocrystals size was achieved compared to what is achieved in literature.[15] This synthesis process was rapid and economical and shows potential for large-scale production. This catalyst design concept provides a new idea to fabricate high-silica HA-ZSM-5 or other zeolites that reveal fast mass transport, which will show a great potential for industrial applications in selective catalytic reactions involved bulky molecules. In this paper, key factors (SiO_2/Al_2O_3 ratio, seed/SiO_2 ratio, and HTAB/SiO_2 ratio) in controlling the crystal size and the morphology of the HA-ZSM-5 zeolites during synthesis have been investigated. Moreover, a possible formation mechanism of the HA-ZSM-5 is also proposed based on experimental observations. The catalytic performance of the representative HA-ZSM-5 (HA-167-2S-5H) were evaluated for the MTP reaction to explore the structure–function relationship. In addition, the catalytic performances of the HA-167-2S-5H zeolite and the blank sample (denoted as C-ZSM-5) without HTAB addition have been compared.

2. Experimental

2.1 Materials

The HA-ZSM-5 zeolite was synthesized by using the following reagents:

Tetraethyl orthosilicate (TEOS, 98.0%, Tianjin Kemiou Chemical Reagent Co.), colloidal silica (SiO_2, 40 wt% suspension in H_2O, Qingdao Haiyang Chemical Reagent Co.), sodium hydroxide (NaOH, 96 wt%, Sinopharm Chemical Reagent Co., Ltd.), sodium aluminate ($NaAlO_2$, 41 wt% Al_2O_3, Sinopharm Chemical Reagent Co., Ltd.), tetrapropylammonium hydroxide

(TPAOH, 25 wt% in H_2O, Shanghai Cairui Chemical Co.), NH_4NO_3 (Sigma-Aldrich), methanol (Tianjin Guangfu Fine Chemical Research Institute Co., Ltd.). n-Hexyltrimethylammonium bromide (HTAB, CP, Tokyo Chemical Industry Co., Ltd.). All reagents were used directly as received and no further purification was conducted.

In addition, a commercial ZSM-5 zeolite ($SiO_2/Al_2O_3 = 167$, denoted as C_1-ZSM-5 and purchased from Nankai Catalyst Plant, Tianjin, China) was used as a reference catalyst to investigate the advantages of the HA-ZSM-5 zeolite in MTP reaction.

2.2 Synthesis of S-1 seeding suspension

S-1 seeding suspension with a final molar composition of $SiO_2 : 0.24$ TPAOH : 24 H_2O : 4 EtOH (in which EtOH was produced from the hydrolysis of TEOS) was prepared using a method developed previously in our lab.[32] The detailed synthesis procedure is as follows: 88.67 g of TPAOH solution was completely dissolved in 130.00 g of H_2O. 97.56 g of TEOS was added dropwise under continuous stirring to the resultant mixture. After stirring for 3 h until a clear solution is obtained (the complete hydrolysis of TEOS), the mixture was then transferred into Teflon-lined stainless steel autoclaves and hydrothermally treated at 105 °C for 48 h in an oven to prepare the seed suspension. The obtained S-1 seeding suspension was directly used as seeds without any centrifugation or washing process.

2.3 Preparation of HA-ZSM-5 zeolite

A typical synthesis of the HA-ZSM-5 zeolite is performed as follows. Firstly, required NaOH, $NaAlO_2$ and deionised water were mixed together with constant stirring, followed by addition of HTAB. Then, different amounts of S-1 seeding suspension was added dropwise to the above clear solution under vigorous stirring. Subsequently, the colloidal silica was added dropwise to the above mixture under stirring and agitated for another 3 h until a homogeneous gel mixture was obtained. In these steps, only a small amount of extra water was added except that contained in the colloidal silica and S-1 seeding suspension. The resultant mixture with a molar composition of 100 $SiO_2 : x$ $Al_2O_3 : 7$ $Na_2O : 1000$ $H_2O : y$ HTAB : z S-1 were transferred into a 50 mL Teflon-lined stainless-steel autoclave and crystallized at 120 °C for 48 h in a furnace with autogenous pressure. After the required time, the solution was quenched with cold water to room temperature and the precipitated products were collected by filtration, washed several times with deionised water until neutral pH was reached, dried overnight at 120 °C and calcined in the air atmosphere at 550 °C for 6 h to remove the organic template, the crystalline product was achieved. Thereafter, three consecutive ion exchange reactions of the calcined Na-form zeolites were carried out at 80 °C for 6 h using a 1.0 M NH_4NO_3 solution. Lastly, the NH_4-form zeolites were isolated by centrifugation, washed with deionised water twice, dried overnight at 120 °C and subsequently calcined at 550 °C for 6 h to obtain H-form zeolites.

The sample obtained is denoted as HA-167 ($SiO_2/Al_2O_3 = 100/0.6 = 167$)-2S-5H, indicating that it was prepared according to the formulation of 100 $SiO_2 : 0.6$ $Al_2O_3 : 7$ $Na_2O : 1000$ $H_2O : 2$ S-1 seed : 5 HTAB at a crystallization temperature of 120 °C and a crystallization time of 48 h.

The C-ZSM-5 zeolite with a molar composition of 100 $SiO_2 : 0.6$ $Al_2O_3 : 7$ $Na_2O : 1000$ $H_2O : 0$ HTAB was crystallized via SSC method under the same condition of HA-ZSM-5 zeolite except that no HTAB was added and made a comparison with the HA-ZSM-5.

The influence of synthesis conditions on resultant HA-ZSM-5 zeolites was studied by changing a parameter while keep the other parameters unchanged. The variation of the synthesis parameters is listed in Table S1 (ESI†). The samples prepared were defined according to the method as mentioned above.

2.4 Characterization

The textural properties of the obtained samples were evaluated from N_2 adsorption–desorption isotherms measured at a liquid nitrogen temperature of −196 °C on a Micromeritics ASAP 2010 analyzer. Each sample was degassed at 300 °C for 4 h before the analysis. The specific surface area (S_{BET}) was determined by the Brunauer–Emmett–Teller (BET) equation. The micropore volume (V_{micro}) and external surface area (V_{ext}) were calculated by the t-plot method and the total pore volume (V_{pore}) was based on the adsorbed amount of N_2 at $p/p_0 = 0.99$. The mesopore volume (V_{meso}) was calculated by subtracting V_{micro} from the corresponding V_{pore}. The pore size distribution (PSD) was estimated by employing the Barrett–Joyner–Halenda (BJH) method from the desorption branch of the isotherm.

The crystal size and morphology were investigated by scanning electron microscopy (SEM) using a JSM-7800F instrument at an operating voltage of 3 kV.

Transmission electron microscopy (TEM) images were collected on a JEM-2100 microscope operating at 200 kV.

The crystalline structures and phase purity were analyzed by X-ray diffraction (XRD) in a Rigaku D/Max 2550V diffractometer using Cu Kα radiation (40 kV, 40 mA), with a scanning angle (2θ) from 5° to 55° at a scanning speed of 8° min^{-1}.

^{29}Si and ^{27}Al MAS NMR measurements were performed to determine the local coordination environments of silicon and aluminum in the ZSM-5 framework on a Bruker Avance III 500 MHz spectrometer. The $Al(NO_3)_3$ and tetramethylsilane (TMS) were adopted as standard references of ^{27}Al and ^{29}Si, respectively.[33,34]

The acid amount and strength were tested by NH_3-temperature programmed desorption (NH_3-TPD) on a Tianjin XQ TP-5076 Auto TPD system. Prior to NH_3 sorption, the H-type sample was carefully outgassed at 400 °C for 0.5 h under He flow to remove the adsorbed moisture, cooled to 100 °C and saturated under NH_3 flow for 20 min. Then, the sample was purged with He for 2 h to remove the physisorbed NH_3 on the surface of the zeolite. Subsequently, NH_3 desorption was carried out between 100 and 600 °C with a linear heating rate of 10 °C min^{-1} in flowing He. The desorbed NH_3 was measured continuously by means of a thermal conductivity detector

(TCD). The TCD signals were calibrated using 10 μL of NH_3 as standard. The number of acid sites was determined from the peak area in their profiles.

The acid sites of the samples were also investigated by pyridine adsorption followed by FTIR spectroscopy. Pyridine adsorption-IR (Py-IR) was conducted on a Vertex 70 IR spectrometer at 4 cm^{-1} resolution. The sample was pressed into thin wafer, and then the wafer was placed in an *situ* cell. The zeolite wafer was degassed for 30 min at 450 °C. A spectrum was recorded as background after the wafer was cooled down to room temperature. Subsequently, pyridine vapour was introduced into the cell until saturation. The spectra were then recorded after evacuation at 200 °C for 1 h. The concentrations of Brønsted (B) acid and Lewis (L) acid were calculated from the peak areas of adsorbed pyridine at around 1540 and 1450 cm^{-1}, and the extinction coefficients of $\varepsilon(B)$ and $\varepsilon(L)$ were 1.88 and 1.42 cm mmol^{-1}, respectively.[35]

Thermogravimetric (TG) analysis was conducted by a SDT600 TGA instrument using a temperature ramp from 30 to 800 °C with a heating rate of 10 °C min^{-1} in an air atmosphere.

2.5 Catalytic performance test

The MTP reaction was carried out at the conditions of 1 atm, 470 °C and WHSV (weight hourly space velocity) = 12 h^{-1} in a continuous flow fixed-bed quartz-tube reactor (8 mm i.d.) heated by a furnace.

Before the reaction, the pressed zeolite (0.5 g, 20–40 mesh) was fixed in the middle section of the tube reactor, with two ends filled with quartz sand. A thermocouple was placed in the center of the catalyst bed for purpose of monitoring the temperature. The quartz tube was positioned in a furnace and aligned ensure that the catalyst was located in the isothermal zone.

Then the catalyst was activated at 470 °C for 1 h under N_2 flow. After that, the liquid feed (methanol/water molar ratio = 1 : 1) was fed into the reactor by a peristaltic pump and purged with N_2.

All products were analyzed online using a gas chromatography (Agilent 7890A) instrument equipped with a flame ionization detector and a DB-1 capillary column (50 m × 0.2 mm × 0.5 μm). To ensure that all products were in the gas phase during the reaction run, the effluent line was heated to 150 °C by a heating belt.

Both methanol and dimethylether (DME) are considered as the unconverted reactants in the calculation.

3. Results and discussion

In order to explore the structure–function relationship, we used the SEM, TEM, XRD, N_2 adsorption–desorption, NH_3-TPD and Py-IR techniques to characterize selected samples.

3.1 Morphology observation and control

As seen in Fig. S1A and B (ESI†), the S-1 seeds prepared by the above mentioned method display an irregular sphere morphology with the crystal sizes of *ca.* 170 nm. The

compositions of the synthetic solutions and the textural properties of resultant samples are listed in Table S1 (ESI†).

The representative SEM images (low and high magnifications), as shown in Fig. 1A and B, exhibit the crystal size and morphology of the HA-ZSM-5 zeolite prepared *via* SSC route. The resultant HA-ZSM-5 zeolite prepared by using HTAB as a mesoscale template exhibits well-separated, ellipsoidal aggregates with a size of 700–800 nm. Their sponge-like exterior surface suggests that they are formed by the aggregation of lots of ultrafine nanocrystals with a particle size of ∼20 nm, which are easily distinguishable through the high-magnification SEM image (Fig. 1B). These nanocrystals size was obviously smaller than that of ZSM-5 aggregates reported in literature.[15]

Comparatively, sample C-ZSM-5 is the one prepared without HTAB addition, which exhibits a mixture of zeolite crystals and amorphous phase (Fig. S2A and B (ESI†)). Zeolite crystals of C-ZSM-5 sample are relatively uniform hexagonal, elongated prismatic shape crystals aggregates with a smoother surface and larger diameter, suggesting that the nanocrystals have fused into large crystals without being stabilized by HTAB.[23] In other words, the C-ZSM-5 zeolite has the typical morphology of large grains with individual crystal sizes of approximately ∼800 nm (Fig. S2A (ESI†)). High-resolution SEM image Fig. S2B (ESI†) displays that the C-ZSM-5 structure is quite compact. The primary unit is elongated prismatic shape crystal with sizes of 400–500 nm in length and 20–30 nm in thickness. In addition, many amorphous materials exist in the C-ZSM-5 sample indicating incomplete crystallization.

In order to further identify the superfine nanocrystals structure, the HA-ZSM-5 zeolites were studied by TEM. The Fig. 2A clearly shows that the HA-ZSM-5 zeolites ($SiO_2/Al_2O_3 =$ 167) with rough surface were agglomerated by many superfine nanocrystals with average sizes of about 15 nm. Superfine nanocrystals of aggregates were clearly seen in the picture. The intercrystal mesoporous distributing homogeneously in the synthesized HA-ZSM-5 zeolite are directly observed from the bright area in the TEM image (Fig. 2A). Clear and parallel lattice fringes spread throughout the entire crystals are visible by the high-resolution TEM image (Fig. 2B) taken at the edge of the HA-ZSM-5 sample, indicating that HA-ZSM-5 zeolites are completely crystalline.[22] The dot pattern of selected area electron diffraction (SAED) of the corresponding HA-ZSM-5 zeolite indicates the single crystalline nature of these nanocrystals (Fig. 2C), which demonstrates that the introduction of mesopores maintains the single crystal integrity.[36,37] Most
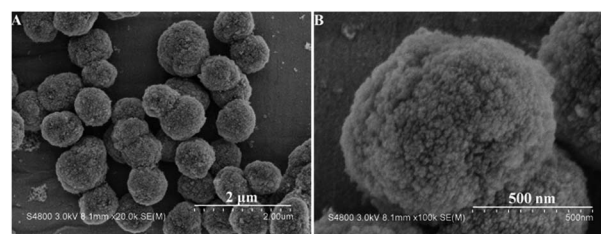

Fig. 1 Low resolution SEM image (A) and high-resolution SEM image (B) of the synthesized HA-ZSM-5 samples.
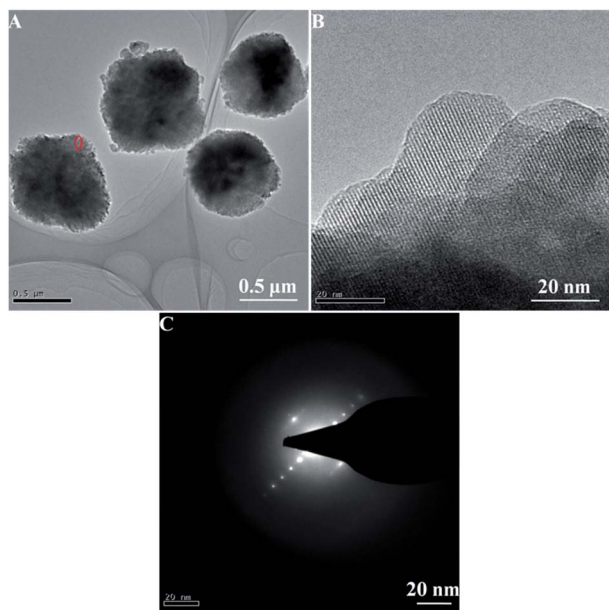
Fig. 2   Low resolution TEM image (A) high-resolution TEM image (B) and the corresponding selected area electron diffraction (SAED) pattern (C) of the synthesized HA-ZSM-5 samples.

importantly, these ultrafine nanocrystals tend to agglomerate into the larger secondary particles with a loose structure, which may be attributed to their high surface Gibbs free energy.[38] The abundant intercrystalline mesopores in the HA-ZSM-5 zeolite were formed by aggregation of ultrafine nanocrystals with sizes of 10–20 nm. In view of the low temperature and short crystallization time used in the synthesis (120 °C and 48 h, respectively), these results indicate the efficiency of this method in the preparation of high quality HA-ZSM-5. However, the low magnification and high magnification TEM images (Fig. S3A–C (ESI†)) of C-ZSM-5 sample show that zeolite crystals were cohered by many amorphous nanoparticles, which is consistent with the results obtained from the SEM images. Besides, no evident mesopores can be seen from the C-ZSM-5 zeolite crystals in the TEM images (Fig. S3A and B (ESI†)).

In order to better control the structure of HA-ZSM-5 zeolites, the influence of the key synthetic parameters, including SiO_2/Al_2O_3 ratio, seed/SiO_2 ratio and HTAB/SiO_2 ratio on the morphology and structure properties of the resultant zeolite was systematically investigated.

Low-magnification SEM images of the HA-ZSM-5 (Fig. S4A–D (ESI†)) reveal that all the samples prepared with different SiO_2/Al_2O_3 ratios present regular ellipsoidal agglomerates with sizes of 600–1000 nm. The aggregates sizes of samples HA-167-2S-5H, HA-200-2S-5H, HA-250-2S-5H and HA-313-2S-5H are 1000, 800, 600 and 550 nm, respectively. Hence, these SEM images indicate that aggregates size of the HA-ZSM-5 decreased as the SiO_2/Al_2O_3 ratio used in the synthetic fluids increased.

However, SEM images under high magnification (inset of Fig. S4A–D, (ESI†)) clearly show that the primary nanocrystals size of HA-ZSM-5 became larger with the increase of SiO_2/Al_2O_3 ratio. For sample HA-167-2S-5H synthesized with SiO_2/Al_2O_3

ratio of 167, the primary nanocrystals were only ~20 nm in size. When the SiO_2/Al_2O_3 ratio was 200, the primary nanocrystals of HA-200-2S-5H sample were ~30 nm in size. At SiO_2/Al_2O_3 ratio of 250, the primary nanocrystals of HA-250-2S-5H sample were ~50 nm in size. Continue to increase the ratio of SiO_2/Al_2O_3 to 313, the primary nanocrystals of HA-313-2S-5H became more larger than HA-250-2S-5H sample (~100 nm in size). This may be attributed to the occurrence of particle–particle fusion when the SiO_2/Al_2O_3 ratio of the synthetic gel increases to a certain value. These results demonstrated that the variation of SiO_2/Al_2O_3 ratio in the synthetic gel has a great influence on the morphology and size of resultant zeolites. A reasonable explanation is that a lower Al-doping content (higher SiO_2/Al_2O_3 ratio) induces a lower coulomb force between HTA+ ions and nanocrystals. The coulomb force is so weak that the synthesis is similar to conventional hydrothermal synthesis, producing relatively large nanocrystals when the SiO_2/Al_2O_3 ratio is relatively high. On the contrary, ultrafine nanocrystals were produced when the SiO_2/Al_2O_3 ratio is relatively low, which is because that the strong coulomb force between HTA+ ions and nanocrystals, inhibiting their excessive growth and the stacking of the ultrafine nanocrystals will form HA-ZSM-5.[23] Besides, lower SiO_2/Al_2O_3 ratio means decreased crystallization rate, leading to the generation of more smaller nanocrystals.[26] These experimental results show that the SiO_2/Al_2O_3 ratio in the synthesis gel is a critical factor in controlling the morphology of HA-ZSM-5.

Fig. S5A–D (ESI†) show the SEM images of the samples prepared with different seed/SiO_2 ratio from 0.005 to 0.06, and SiO_2 in the seeding suspension took up 0.5% (seed/SiO_2 ratio = 0.005), 2% (seed/SiO_2 ratio = 0.02), 4% (seed/SiO_2 ratio = 0.04) and 6% (seed/SiO_2 ratio = 0.06) of the SiO_2 in the total batch. SEM observations (Fig. S5A–D (ESI†)) clearly show that all the samples exhibit ellipsoidal aggregates consisting of superfine nanocrystals ranging from 20 to 70 nm. As can be seen from the SEM images in Fig. S5A–D (ESI†), the aggregates size of the HA-ZSM-5 decreases from 1000 nm to 850 nm with increasing seed/SiO_2 ratio from 0.005 to 0.06.

By adding 0.5% of seeds, the gel of HA-167-0.5S-5H rapidly crystallizes to large ellipsoidal aggregates with a rough surface and a particle size of 1000 nm (Fig. S5A, ESI†), indicating that the obtained gel can be quickly converted into HA-ZSM-5 zeolite when the seed/SiO_2 ratio is only 0.005. The aggregates size of HA-167-2S-5H remains unchanged when the seed amount increases to 2% (Fig. S5B (ESI†), HA-167-2S-5H). When more seeds (4%) are added, zeolite HA-167-4S-5H has a smaller aggregates size of about 950 nm (Fig. S5C (ESI†), HA-167-4S-5H). The aggregates size dramatically decreased from ~950 nm to smaller than 850 nm when the seeds amount further increased up to 6%.

However, the primary nanocrystals size decreased first and then increased with the increasing of the seed/SiO_2 ratio (inset of Fig. S5A–D, ESI†). The primary nanocrystals size of HA-167-0.5S-5H were as large as 70 nm when the seed/SiO_2 ratio was 0.005. However, the size of the primary nanocrystals decreased sharply from 70 nm to less than 20 nm with the seed/SiO_2 ratio increasing from 0.005 to 0.02. As observed in the inset of

Fig. S5A–D,† the smallest nanocrystals size has been obtained in the case of seed/SiO$_2$ = 0.02. This may be attributed to the seeds to provide appropriate amount of surfaces to induce the nucleation, and then affect the growth and aggregation of crystal nucleus, leading to a sharp decrease in primary nanocrystals size of HA-ZSM-5. A further increase of the ratio of seed/SiO$_2$ up to 0.04 and 0.06, the relatively higher seed/SiO$_2$ ratio may cause a high growth rate and the seeds had very little time to be dissolved and/or fragmented into small species and then produce secondary nuclei,[15] and therefore the primary nanocrystals of HA-313-4S-5H and HA-313-6S-5H became more larger than that of the aforementioned two samples (HA-313-0.5S-5H and HA-313-2S-5H) (inset of Fig. S5C and D, (ESI†)). Therefore, coordinating the process of growth and nucleation is very critical for the preparation of HA-ZSM-5. One extreme end (seed/SiO$_2$ = 0.06) is that the growth process is too fast to produce secondary nuclei and the other end (seed/SiO$_2$ = 0.005) is the incomplete crystallization of synthetic gel when it progresses too slowly.

As we all known, the basic behaviors of seeds are to provide surface for the synthetic gel and to induce the production of a large number of secondary nuclei after their partial dissolution.[39–41] In the present study, the obvious difference between the S-1 seeds (Fig. S1A (ESI†)) and primary nanocrystals of HA-ZSM-5 zeolites (Fig. S5B†) confirms the above-mentioned results. These nuclei are thought to play a guiding role in the formation of the target crystalline phases. Consequently, the crystallization time is greatly reduced.

In summary, the employed amount of S-1 seeds has an important influence not only on the aggregates but also on the primary nanocrystals of the HA-ZSM-5 zeolites.

Fig. S6A–D (ESI†) display the SEM images of the samples prepared with different HTAB/SiO$_2$ ratios. As shown in the SEM images, all the samples exhibit regular ellipsoidal aggregates whose size varies in the range of 1100–1300 nm and one can see the difference in aggregates size and morphology with the increase of the HTAB/SiO$_2$ ratio. The aggregates size of the HA-ZSM-5 zeolites increased first and then decreased with the increasing of the HTAB/SiO$_2$ ratio.

When the HTAB/SiO$_2$ ratio was less than 0.05, a mixture of amorphous material and HA-ZSM-5 zeolites was obtained (Fig. S6A and B (ESI†)). This may be attributed to the strength of coulombic interaction between HTA$^+$ ions and nanocrystals was too weak to stabilize the zeolite nanocrystals. The dandelion-like HA-ZSM-5 zeolites were produced when the HTAB/SiO$_2$ ratio was above 0.03, which is attributed to the addition of suitable HTAB. Because the HTAB can stabilize the superfine nanocrystals by lowering their surface Gibbs free energy, enabling the formation of highly crystalline HA-ZSM-5 zeolites at short notice.[23]

At the relatively low HTAB/SiO$_2$ ratios from 0.01 to 0.05 (the inset of Fig. S6A–C (ESI†)), the primary nanocrystals sizes of HA-ZSM-5 zeolites gradually decrease from 170 nm to 20 nm. With further increase in HTAB/SiO$_2$ ratio up to 0.07, the primary nanocrystals size of the HA-167-2S-7H became larger than that of HA-167-2S-5H, which may be because that the strength of interaction between HTA$^+$ ions and nanocrystals is so strong

that the self-assembly process gets disturbed. In spite of this, primary nanocrystals sizes of the four samples are much smaller than that of C-ZSM-5 (Fig. S2†). Moreover, when HTAB was used, the morphology of the synthesized HA-ZSM-5 (Fig. S6A–D (ESI†)) becomes significantly different from that of C-ZSM-5 (Fig. S2 (ESI†)).

In light of this, the employed amount of the HTAB has a major influence on the crystal size and morphology of resultant HA-ZSM-5 zeolites. It is worth emphasizing that the coulomb force between HTAB and nanocrystals must be in a suitable range; if the coulomb force is too strong, the self-assembly process of nanocrystals will be affected, if the coulomb force is too weak, it will be unfavourable for zeolites crystallization and cannot stabilize the ultrafine nanocrystals. Therefore, HTAB/SiO$_2$ ratio in the synthetic gel is very important for the preparation of ultrafine HA-ZSM-5 zeolite.

The above results show that the morphology and primary nanocrystals size of HA-ZSM-5 zeolite can be controlled by changing the key synthetic parameters of the synthetic solution.

3.2 Textural properties and crystallinity

Fig. 3A and B show the N$_2$ adsorption–desorption isotherms and the corresponding PSD curves of C-ZSM-5 and HA-ZSM-5 zeolites prepared with different SiO$_2$/Al$_2$O$_3$ ratios. As seen in Fig. 3A, the high uptake steps at relatively low pressure ($p/p_0 <$ 0.02) are observed in the N$_2$ isotherms (Fig. 3A) of HA-ZSM-5, indicating the high microporosity in the single-crystalline HA-ZSM-5 samples.[42] In addition, all the samples with different of SiO$_2$/Al$_2$O$_3$ ratios exhibit the characteristic features of a combination of type I + IV isotherms, an obvious hysteresis loop which was associated with capillary condensation at $p/p_0 = 0.45$–0.99 taking place in the open mesopores, evidencing that the intercrystal mesopores have been formed in the HA-ZSM-5 zeolites.[43] Moreover, these adsorption and desorption isotherms exhibit large parallel disposition, further indicating the presence of open mesopores connected to the external surface.[44] To a certain extent, it's easier for the open mesopores to reduce the diffusion limitations for large molecules to escape compared to cavities of pores.[45]

It is worthwhile to note that a unusual hysteresis loop in the N$_2$ isotherm of the sample HA-250-2S-5H is visible at low relative pressure between 0.10 and 0.30, which is ascribe to a fluid-to-crystalline phase transition of the adsorbed nitrogen in microporosity.[46] This special phenomenon demonstrates that the nanocrystals of the sample HA-250-2S-5H are well crystallized.[47] The hysteresis loop inseparably linked with fluid-to-crystalline phase transition gets larger for the high silica HA-313-2S-5H zeolite.

The PSD curves of samples obtained with different SiO$_2$/Al$_2$O$_3$ ratios reveal that the HA-ZSM-5 contained mesopores of a relatively broad size distribution between 3 and 9 nm peaked at 3.8 nm. In addition, the mesopore size of the HA-ZSM-5 zeolite became smaller and narrower with increasing the SiO$_2$/Al$_2$O$_3$ ratio from 167 to 313 (Fig. 3B).

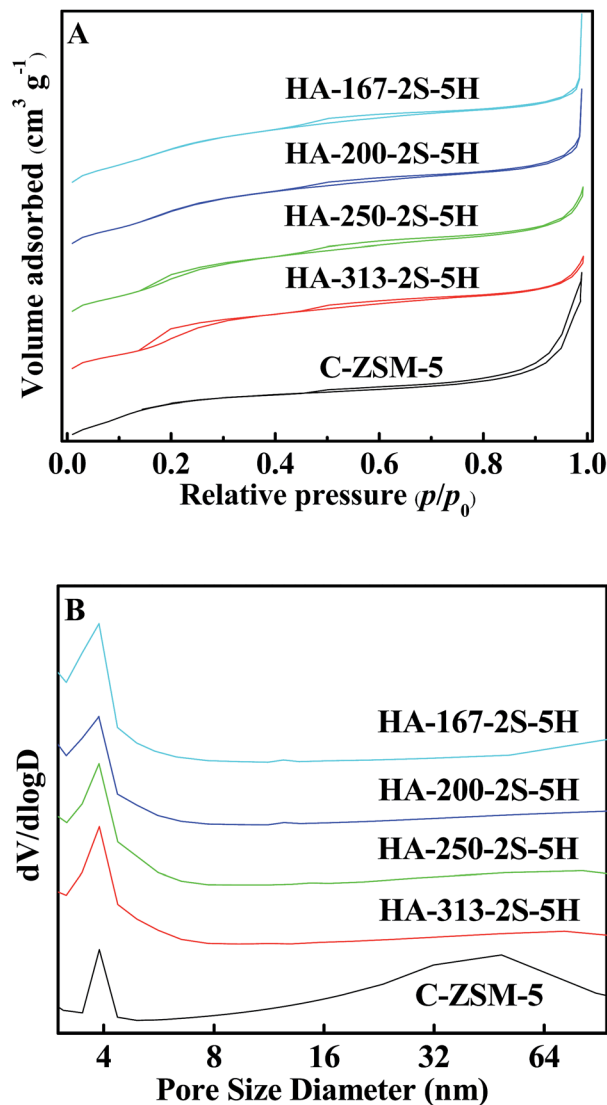Comparatively, the C-ZSM-5 sample also displays a combination of type I + IV isotherm, which was associated with the

Fig. 3 N$_2$ adsorption isotherms (A) and PSD curves (B) of the HA-ZSM-5 zeolites with different SiO$_2$/Al$_2$O$_3$ ratios.

capillary condensation at the high relative pressure taking place in the open mesopores. In addition, C-ZSM-5 shows a low uptake step in micropore range indicating the presence of a small quantity of micropores (V_{micro} listed in Table S1† only 0.06 g cm^3). The PSD curve of C-ZSM-5 demonstrates that the sample has bi-modal porosity within the range of 3.5–4.4 nm and 6–90 nm (Fig. 3B). Nevertheless, it is worth noting that the mesopores or macropores of C-ZSM-5 mainly came from small sized amorphous materials.

The detailed texture properties of zeolite samples are depicted in Table S1 (ESI†). As shown in the Table S1 (ESI†), the increase of the SiO$_2$/Al$_2$O$_3$ ratios (from 167 to 313) caused greatly decrease of both S_{BET} and V_{pore}, especially for the V_{meso}. With increasing the SiO$_2$/Al$_2$O$_3$ ratio from 167 to 313, V_{meso} decreased from 0.19 cm^3 g^{-1} to 0.16 cm^3 g^{-1} (Table S1, ESI†). These results can be explained by the presence of particle–particle fusion with the increase of the SiO$_2$/Al$_2$O$_3$ ratio, which are well in agreement with the previous reports.[15] However, C-ZSM-5 has a smaller

adsorption capacity compared with HA-ZSM-5 zeolites. First of all, it has a lower V_{pore} than that of the HA-ZSM-5 zeolites. Also, the S_{BET}, S_{ext} and V_{micro} of HA-ZSM-5 (403 m^2 g^{-1}, 217 m^2 g^{-1} and 0.09 cm^3 g^{-1}) are higher than that of C-ZSM-5 (311 m^2 g^{-1}, 167 m^2 g^{-1} and 0.06 cm^3 g^{-1}), with the increasing of 30% and 50%, which could be ascribed to the high crystallinity, high purity and hierarchical structure of HA-ZSM-5. Then again, the V_{micro} of C-ZSM-5 is much lower than HA-ZSM-5 firmly indicating that C-ZSM-5 sample may contain amorphous materials.

Fig. 4 shows the powder XRD patterns of C-ZSM-5 and HA-ZSM-5 zeolites prepared with different SiO$_2$/Al$_2$O$_3$ ratios from 167 to 313. All the samples exhibit the typical diffraction peaks associated with MFI topology, confirming the successful synthesis of HA-ZSM-5 zeolites through SSC route. No other crystalline phases were detected. The relative crystallinity was calculated by the peak areas between $2\theta = 7$–$10°$ and 22–$25°$ based on the standard sample C-ZSM-5, and the computing results are summarized in Table S1 (ESI†). The relative crystallinity are 107, 108, 109 and 110 for HA-167-2S-5H, HA-200-2S-5H, HA-250-2S-5H and HA-313-2S-5H, respectively, based on the reference crystallinity 100 of C-ZSM-5. Namely, the relative crystallinity of HA-ZSM-5 samples increased as the SiO$_2$/Al$_2$O$_3$ ratio increased. The relative crystallinity of the C-ZSM-5 is lower than that of the HA-ZSM-5 zeolites, which is due to their different crystal sizes and morphologies formed by different synthesis conditions. This result is consistent with the SEM and N$_2$ sorption studies, demonstrating the incomplete crystallization of C-ZSM-5.

Fig. S7A and B (ESI†) display the N$_2$ adsorption–desorption isotherms and PSD curves of the HA-ZSM-5 zeolites prepared with different seed/SiO$_2$ ratios. As shown in Fig. S7A,† all the samples exhibit a hybrid of type I and IV isotherm with some variations in the hysteresis loops. In the isotherms, a sharp uptake at $p/p_0 < 0.02$ is associated with microporosity present in the zeolites. All the samples exhibit clear hysteresis loops at high relative pressure in the range of 0.45–0.99, which mainly attributes to the capillary condensation in the open mesopores.
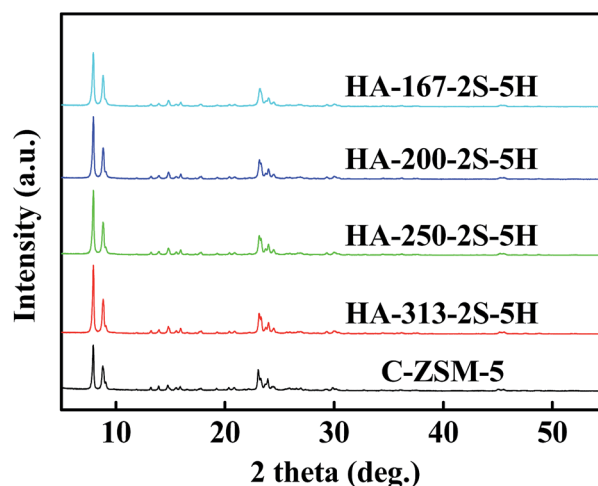

Fig. 4 XRD patterns of the C-ZSM-5 and HA-ZSM-5 zeolites with different SiO$_2$/Al$_2$O$_3$ ratios.

The presence of mesopores is further confirmed by PSD curves of HA-ZSM-5 samples. As is seen in Fig. S7B,† HA-ZSM-5 zeolites apart from HA-167-6S-5H sample have narrow PSD in the short range of 3–9 nm. Among these, HA-167-0.5S-5H has the sharpest and narrowest PSD. In addition, all the samples exhibit a sharp band centered at *ca.* 3.8 nm. This band width first increased and then decreased with increasing the seed/SiO_2 ratios from 0.005 to 0.04. Moreover, PSD curve of the sample HA-167-2S-5H exhibits the highest intensity of the band centered at *ca.* 3.8 nm. This result may be due to the presence of the smallest nanocrystals of HA-167-2S-5H sample. Significantly, HA-167-6S-5H sample exhibits a more intense band centered at *ca.* 50 nm in addition to a smaller one at *ca.* 3.8 nm. The relative large secondary pores or macropores probably resulted from the void space between the randomly aggregated larger secondary particles.[38,48]

The textural data are listed in Table S1 (ESI†). With increasing the seed/SiO_2 ratios from 0.005 to 0.06, the S_{ext}, V_{pore}, and V_{meso} first increased and then decreased, and at a seed/SiO_2 ratio of 0.02, the peak values appeared. The HA-167-2S-5H zeolite exhibits the highest S_{ext} of 201 m^2 g^{-1} and V_{meso} of 0.19 cm^3 g^{-1}, which can apparently be attributed to its ultrafine nanocrystals with sizes of ∼20 nm.

The differences of texture properties can be attributed to their different morphologies and nanocrystals sizes. The primary nanocrystals sizes decreased first and then increased as the seed/SiO_2 ratios increase; hence the intercrystal mesopores constructed upon the aggregation of ultrafine nanocrystals first increased and then decreased, which result in the variations of isotherms and the corresponding textural properties.[16]

The XRD patterns of HA-ZSM-5 samples prepared with different seed/SiO_2 ratios from 0.005 to 0.06 are depicted in Fig. S8 (ESI†). These patterns indicate that the high-purity and high crystallinity HA-ZSM-5 were produced, with no evidence of the formation of other crystalline phases. The relative crystallinity of the resultant HA-ZSM-5 decreases at first and then increases as the seed/SiO_2 ratio increasing from 0.005 to 0.06 (Table S1, (ESI†)). This result is mainly due to the different nanocrystals sizes of the four samples. The smaller the nanocrystals size, the lower the degree of relative crystallinity. So the HA-167-2S-5H sample with the smallest nanocrystals size of ∼20 nm exhibits the lowest relative crystallinity.

The N_2 adsorption–desorption isotherms and the PSD curves of the HA-ZSM-5 zeolites synthesized with different HTAB/SiO_2 ratios from 0.01 to 0.07 are presented in Fig. 5A and B. All the samples present combined types I and IV isotherm. The high uptake steps in the low relative pressure region of $p/p_0 < 0.01$ are observed, which indicates that micropores are present. Moreover, the hysteresis loops at $p/p_0 = 0.45$–0.99 are considered as capillary condensation in the open mesopores, indicating the hierarchical structure of the resultant samples.

As shown in Fig. 5B, HA-167-2S-1H zeolite shows a bimodal distribution with the porosity around 3.4–4.4 nm and 4.4–30 nm. However, the PSD curves can't reflect the real aperture distribution when the HTAB/SiO_2 ratio from 0.00 to 0.01, because the mesopores of C-ZSM-5 and HA-167-2S-1H partly came from small sized amorphous materials due to their
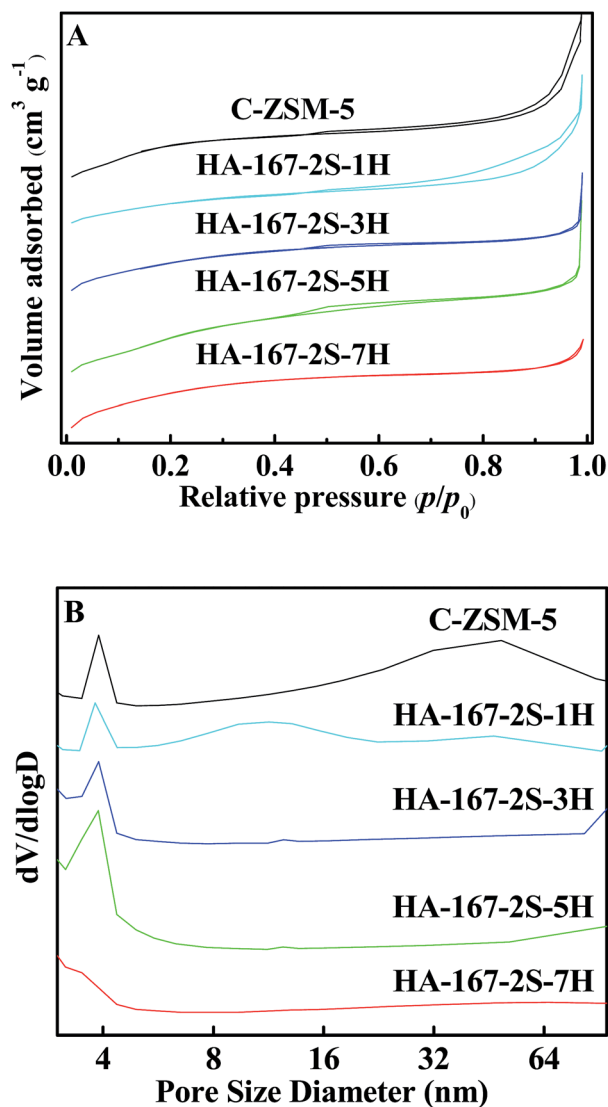

Fig. 5 N_2 adsorption isotherms (A) and PSD curves (B) of the HA–ZSM-5 zeolites with different HTAB/SiO_2 ratios.

incomplete crystallization. Varying the HTAB/SiO_2 ratio from 0.03 to 0.07, the PSD of mesoporous broaden first and then narrowed. As can be seen, the sample HA-167-2S-3H shows a small and narrow peak in the range of 3.4–4.4 nm centered at 3.8 nm, however, HA-167-2S-5H sample exhibits the higher and broader peaks in the range of 3–9 nm centered at around 3.8 nm, reflecting its increasing mesoporosity. Like HA-167-2S-3H, the sample HA-167-2S-7H also shows a small and narrow peak in the range of 3–5 nm centered at 3.5 nm and the presence of mesopores is negligible, which is consistent with its N_2 adsorption–desorption isotherms.

As is seen in Table S1 (ESI†), the S_{BET}, S_{ext}, V_{pore} and V_{meso} of HA-ZSM-5 samples are increases at first then decreases with increasing the HTAB/SiO_2 ratio from 0.01 to 0.07. In the absence of HTAB, the C-ZSM-5 sample has the lowest S_{BET} and V_{micro} (Table S1 (ESI†)) among the five samples. With increasing the HTAB/SiO_2 ratio from 0.00 to 0.03, the V_{micro}, the S_{BET} are increased and the V_{meso} is decreased, which further validate the

incomplete crystallization of C-ZSM-5, HA-167-2S-1H and HA-167-2S-3H samples. It is due to the fact that without enough HTAB in the synthesis gel leading to crystallization process progresses too slow to completely crystallization of amorphous phase, which are consistent with the SEM images (Fig. S2, S6A and B†). Moreover, the V_{pore} of the sample HA-167-2S-5H (0.29 cm^3 g^{-1}) was higher than the other two samples (0.23 cm^3 g^{-1} for HA-167-2S-1H, 0.24 cm^3 g^{-1} for HA-167-2S-3H), which was attributed to its large mesopore volume. Furthermore, the sample HA-167-2S-7H has the lower S_{BET} and V_{pore} than that of HA-167-2S-5H, which is because that excessive HTAB influenced the self-assembly process of HA-ZSM-5 zeolites. Thus, the addition of excess HTAB in the synthetic solution is unfavourable for the formation of HA-ZSM-5 zeolites.

Fig. 6 displays the XRD patterns of HA-ZSM-5 zeolites prepared with different HTAB/SiO$_2$ ratios from 0 to 0.07, from which it could be seen that the typical diffraction peaks of the MFI structure were identified for all the samples. No other zeolitic phases were observed. Notably, the sample C-ZSM-5 synthesized without HTAB addition has a low crystallinity despite all other conditions being the same (Fig. 6 and Table S1 (ESI†)). On varying the HTAB/SiO$_2$ ratio from 0.01, 0.03 and 0.05 to 0.07, the relative crystallinity of the synthesized HA-ZSM-5 zeolites enhanced first and then decreased.

As can be seen from Table S1 (ESI†), the relative crystallinity of HA-167-2S-1H, HA-167-2S-3H, HA-167-2S-5H and HA-167-2S-7H were 81%, 100%, 107% and 102%, respectively.

HA-167-2S-5H and HA-167-2S-7H appeared to be highly crystalline, whereas HA-167-2S-1H and HA-167-2S-3H samples were less-crystalline with the significant presence of amorphous phase, which can be attributed to the difference of the coulomb force between HTAB and nanocrystals at different HTAB/SiO$_2$ ratios. When the HTAB/SiO$_2$ ratio is less than 0.05, the HA-167-2S-1H and HA-167-2S-3H samples show low relative crystallinity, which could be mainly attributed to their incomplete crystallization caused by few amounts of HTAB. As the HTAB/SiO$_2$ ratio was increased to 0.05, the relative crystallinity of the

prepared HA-167-2S-5H was higher than HA-167-2S-1H or HA-167-2S-3H. Further increasing the HTAB/SiO$_2$ ratio from 0.05 to 0.07 saw a progressive decrease in the intensity of the MFI diffraction peaks. This is consistent with the results reported in the literature.[49] One reasonable explanation is that S-1 seeds and HTAB are a competitive relationship, not a cooperative relationship under our experimental conditions. Although a large amount of mesoporous phase can be produced by adding excess HTAB to the synthetic solution, crystallization rate is so slow that cannot ensure the transformation completely from original mesoporous phase to the desired HA-ZSM-5. So, the presence of unconvertible mesoporous materials leads to a low relatively crystallinity of HA-167-2S-5H sample.

3.3 ^{27}Al and ^{29}Si MAS NMR analysis

In order to study the local coordination environments of silicon and aluminum and investigate whether all the silicon and aluminum are incorporated in the framework, ^{29}Si and ^{27}Al MAS NMR experiments of the representative HA-ZSM-5 (here, the sample HA-167-2S-5H was used as a representative) were carried out with the spectra as shown in Fig. 7A and B. The MAS ^{29}Si NMR spectra of the calcined HA-167-2S-5H zeolite (Fig. 7A) exhibits a strong resonance with a chemical shift at −112 ppm, which are associated to Si(OSi)$_4$ (4Si, 0Al) silica species in the HA-167-2S-5H zeolite framework. The weak shoulder peak at −105 ppm can be attributed to (AlO)–Si(OSi)$_3$ (3Si, 1Al) species. No signal was detected at = −100 ppm and = −92 ppm, indicating that (HO)Si(OSi)$_3$ (3Si, 1OH) and (HO)$_2$Si(OSi)$_2$ (2Si, 2OH) silicate species are not present in the HA-167-2S-5H sample.[50]

^{27}Al MAS NMR is a very effective technique to investigate the coordination state of Al species. As shown in Fig. 7B, the MAS ^{27}Al NMR spectrum of calcined HA-167-2S-5H zeolite displays a very strong resonance with a chemical shift at 55 ppm, which is attributed to the tetrahedral-coordinated framework Al with four Al–O–Si bonds.[51] No signal was detected at about 0 ppm, which indicates that no octahedral extra framework aluminum existed in the final product, *i.e.*, all Al atoms have been bonded into the crystal frameworks of the HA-167-2S-5H zeolite.[52] The absence of extraframework octahedral Al atoms further confirmed the high crystallinity of the HA-167-2S-5H sample. All these results demonstrate that the HA-167-2S-5H zeolite synthesized *via* SSC route show high crystallinity with a good distribution of the Al species.

3.4 Surface acidity measurement

The nature and distribution of acid sites are very important for the catalytic performance of the catalyst. Hence, we compared the acid sites and acid strength of HA-167-2S-5H and C-ZSM-5 samples. As shown in Fig. 8, both samples exhibit two evident desorption peaks at 189 °C and 400 °C representing weak and strong acid sites, respectively. The TPD peak area represents the amount of ammonia desorbed from the acid sites of the catalysts, which is proportional to the number of acid sites. Values of the sample acidity are given in Table S2 (ESI†). As can be seen from Table S2 (ESI†), both the concentration of weak acid sites and strong acid sites for HA-167-2S-5H are lower than that of C-
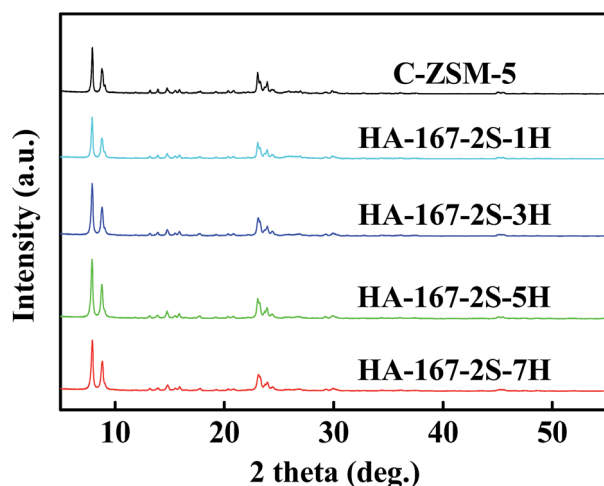
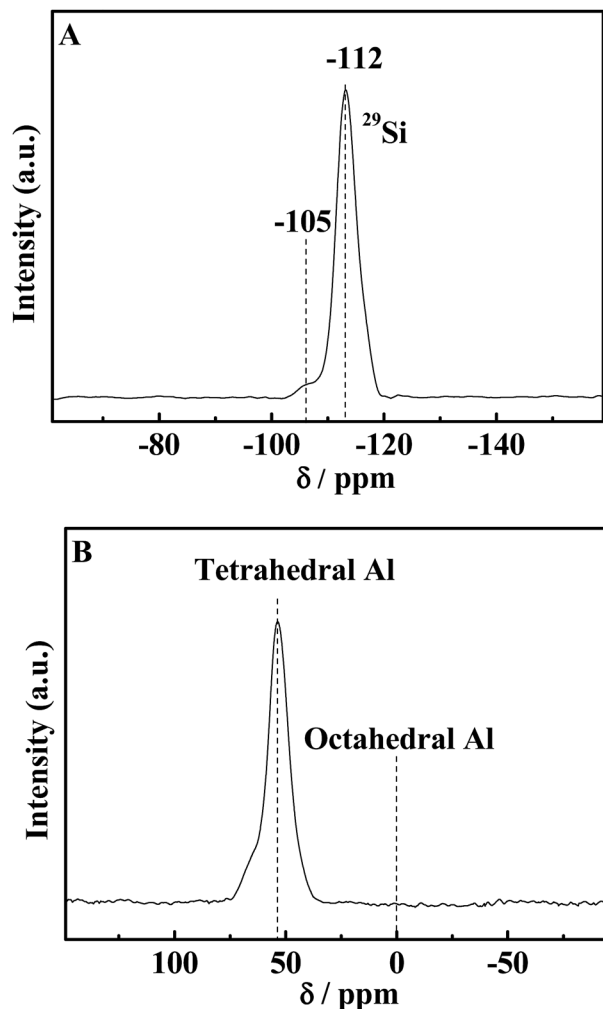**Fig. 6** XRD patterns of the HA-ZSM-5 zeolites synthesized using different HTAB/SiO$_2$ ratios.

Fig. 7 ^{29}Si MAS NMR (A) and ^{27}Al (B) spectra of HA-167-2S-5H sample.

Fig. 8 NH_3-TPD profiles of the HA-ZSM-5 and C-ZSM-5 zeolites.
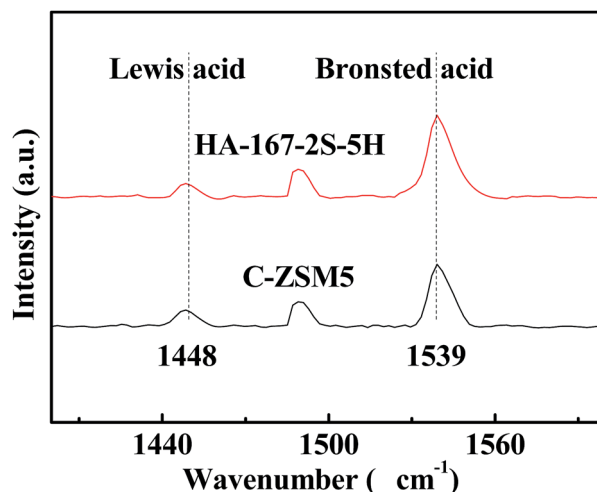
Fig. 9 Py-IR spectra of the HA-167-2S-5H and C-ZSM-5 zeolites.

ZSM-5. The probable reason for the weak acid strength of HA-167-2S-5H zeolite is that the presence of HTA$^+$ partially inhibits the aluminum from incorporating into the framework of the zeolite.

The nature of acidity was further characterized by using pyridine-absorbed FTIR experiments (Fig. 9), in which the vibration band at 1448 cm^{-1} was associated with Lewis (L) acid sites, while the band at 1539 cm^{-1} was attributed to the vibration of pyridine molecules adsorbed on Brønsted (B) acid sites. The concentrations of B acid and L acid were calculated by the areas of the peaks at 1539 and at 1448 cm^{-1}, respectively, and the computing results are listed in Table S3 (ESI†). As observed in Fig. 9 and Table S3 (ESI†), the B acid concentration of HA-167-2S-5H sample is higher than that of the C-ZSM-5 sample, while the L acid concentration of HA-167-2S-5H sample is much lower than that of the ZSM-5 sample, which can be attributed to the sample's unique structure framework.

Based on the above results, we can conclude that the addition of HTAB into the synthetic solution can also adjust the concentration of B acid and L acid and the distribution of acid sites, in addition to stabilizing ultrafine nanocrystals.
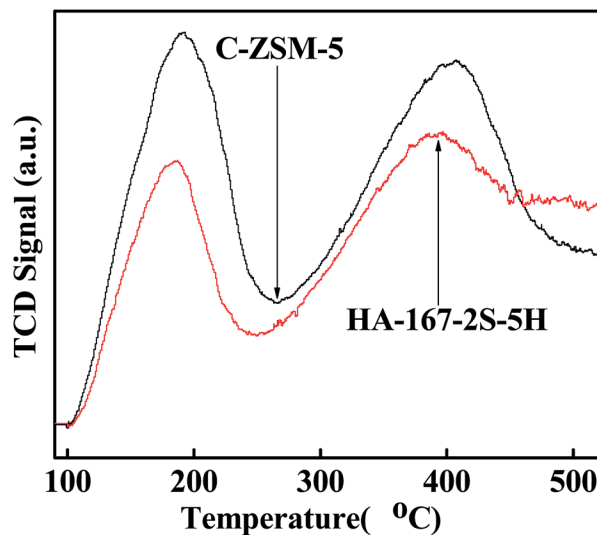
3.5 Catalytic performance

In this study, the MTP reaction was selected as a probe reaction to demonstrate the superiority of HA-ZSM-5. The HA-167-2S-5H, C-ZSM-5 and C$_1$-ZSM-5, with the same SiO$_2$/Al$_2$O$_3$ ratio (167) were comparatively evaluated under identical conditions. One thing to note is that in order to compare the catalysts quickly, the MTP reaction was carried out at high WHSV (12 h^{-1}), much higher than that required in industry (about 1 h^{-1}).[17] A few hours longer of the catalyst lifetime in the evaluation means much longer catalyst life in the commercial reactors.

Catalytic activity *versus* time on stream over HA-167-2S-5H, C-ZSM-5 and C$_1$-ZSM-5 samples is displayed in Fig. 10. At the initial reaction stage, all studied catalysts present a high initial activity of approximately 100%, probably due to the availability of the most acid sites for methanol.[53] However, as the reaction proceeds, all selected catalysts are reducing their catalytic activity with different deactivation rates, which was also likely
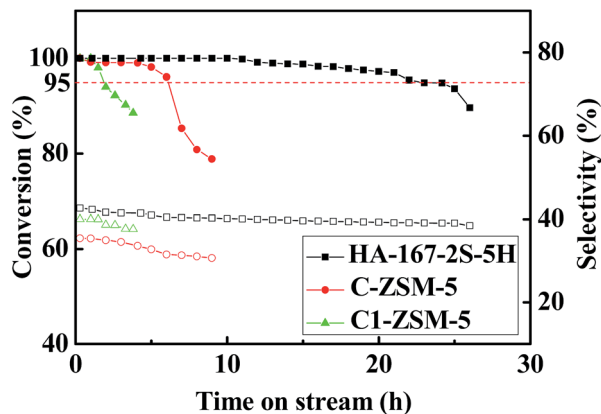
Fig. 10 Methanol conversion and selectivity *vs.* reaction time: $T = 470\ °C$, $P = 1\ bar$, n (methanol) : n (water) $= 1:1$, WHSV $= 12\ h^{-1}$.

attributed to the different coverage of acid sites and blockage of the zeolite channels by coke deposit.[54,55] Here, the catalytic lifetime of catalyst is set as the running time at which methanol conversion above 95%, which is marked with a dashed line in Fig. 10. As seen, their catalytic lifetime follows 22 h, 6 h and 1.5 h with order of HA-167-2S-5H > C-ZSM-5 > C₁-ZSM-5. The HA-167-2S-5H maintains prominent catalytic stability and its catalytic lifetime is nearly 3.7 and 14.7 times longer than that of the C-ZSM-5 and C₁-ZSM-5, respectively. However, C-ZSM-5 exhibits a faster deactivation and presents the shorter lifetime compared to HA-167-2S-5H. Especially, C₁-ZSM-5 deactivated very quickly and presents the shortest lifetime among all the studied catalysts.

The average selectivities of the products at steady stage are listed in Table S4 (ESI†). Clearly, in comparison with the C-ZSM-5 and C₁-ZSM-5, the HA-167-2S-5H exhibits the highest selectivities toward light olefins ($C_2^=-C_4^=$ (68.5%)), butylenes (22.9%) and propylene (40.1%), while their selectivities toward ethylene (5.5%), C_1-C_4 alkanes (3.7%) and C_5^+ hydrocarbons (27.8%) are lowest (Table S4, ESI†), thus resulting in the highest ratio of propylene/ethylene (P/E = 7.3). The average propylene selectivity of the HA-167-2S-5H sample at steady stage reaches as high as 40.1%, 7.0% and 1.4% higher than that of the C-ZSM-5 and C₁-ZSM-5, respectively.

The obvious difference in the catalytic activities for MTP reaction over the HA-167-2S-5H, C-ZSM-5 and C₁-ZSM-5 samples can be explained by their different structural properties (PSD and channel length) and acidic properties (the number, strength and accessibility of the acid sites).[56]

Firstly, the superfine nanocrystals of well-crystallized HA-167-2S-5H prepared with HTAB addition shorten the diffusion path of methanol and products, increasing the active sites accessibility and reducing the diffusional limitations for various products to escape, which could effectively suppress the formation of higher olefins, paraffins and aromatics and could play a more important role in desired products selectivities enhancement. In addition, for the HA-167-2S-5H catalyst with intercrystal mesopores, carbon deposition is mainly formed at the outer surface and/or mesopores.[57] Hence, the large surface

area, high mesopore volume and short diffusion path of HA-167-2S-5H facilitate the removing of primary products and the coke precursor from the active centers of the catalysts, and then reduce the secondary reactions for hindering coke deposition.

Earlier studies have proved that the weak acid sites resulted in the conversion of methanol to DME while the strong acid sites resulted not only in the conversion of DME (and methanol) to light olefins but also side products (polyolefins, aromatic compounds and carbon deposits).[58,59] Additionally, the strong acidity also enhances coke formation and catalyst deactivation,[60] whereas the weak acidity could efficiently restrain various side-reactions for depressing coke deposition.[59] So, both the weak acid sites and strong acid sites are of equal importance and the strong to weak acidity ratio has a significant impact on catalytic activity of catalysts in MTP reaction.

The relatively low total acid amount of HA-167-2S-5H sample (Fig. 8 and Table S2 (ESI†)) hinders side reactions (alkylation, isomerization, hydrogen transfer, and aromatization and so on) on strong acid sites, decreasing coke formation and retarding catalyst deactivation.[56] So the lowered acid strength of the HA-167-2S-5H sample is responsible for its prominent catalytic stability. Again, considering the lowest content of the C_5^+ compounds produced on the HA-167-2S-5H, it was reasonable to conclude that the formation of coke deposition in zeolite was suppressed.[61]

Moreover, the enhanced stability of the HA-167-2S-5H can also be attributed to its excellent accessibility of acid sites. Consequently, secondary reaction, which will eventually lead to coking, is largely restrained. So the appropriate total acid amount and superior accessibility are also responsible for its enhanced catalytic lifetime. Hence, weak carbon deposition and weak sensitivity to more carbon deposits slowed the deactivation of the HA-167-2S-5H, which will be favorable to the operation of the long-term methanol conversion.

Besides, it is well known that the most B acid sites are located in the micropores of the ZSM-5 and closely related to the suppression of the secondary reactions, it thus has unique shape selectivity.[62] So, the HA-167-2S-5H catalyst presents the high propylene selectivity possibly because of its appropriate B acidity and B/L ratio,[61] but meanwhile the relatively low total acid amount is a critical factor for its long catalytic lifetime (Tables S2 and S3 (ESI†)).

As a consequence, the synergistic effects of the excellent structural properties, appropriate acidity, suitable strong/weak acid sites ratio, good accessibility of acidic sites and high crystallinity contribute to the enhancement of the catalytic performance.

In contrast, the C-ZSM-5 sample synthesized without HTAB addition only delivered a lifetime of 6 h under the identical conditions. As mentioned earlier, detailed characterization have confirmed that (SEM, TEM, XRD and BET analysis) C-ZSM-5 sample has a low crystallinity and only a portion of this material possesses small-sized micropores which contain low B acid amount. Note that no mesopores can be formed in zeolite crystals of C-ZSM-5 and the mesopores or macropores mainly came from small sized amorphous materials. Moreover, large crystal particles of C-ZSM-5 sample lead to longer diffusion

paths, increasing diffusion limitations for various products to spread out and decreasing the active site accessibility. Hence, the pure microporosity of C-ZSM-5 zeolite cannot afford the transport and diffusion of bulky substrates within the intra-zeolitic space, and thereby the reaction-produced products with larger molecular sizes would be more likely to become trapped and eventually lead to carbon deposition. So, the solely micro-porous C-ZSM-5 catalyst is progressively deactivated as the micropores are filled with coke deposits, or their channels become blocked.[63] Hence, the microporous C-ZSM-5 catalyst is not capable of enduring higher space velocity for a longer period of time than the HA-167-2S-5H catalyst.

It is believed that the excellent textural properties are the key to afford a long catalytic lifetime and a high propylene selectivity in the MTP reaction. Otherwise, the high density of acid sites will accelerate coking, i.e. deactivation.[59] Hence, in this study, the high value of L acid sites of C-ZSM-5 may bring about the rapid deactivation. Aiming to investigate this possibility, the mixture of C-ZSM-5 and mesoporous SiO_2 (denoted as C_2-ZSM-5) was tested in MTP under the same conditions as C-ZSM-5 for comparison in catalytic performance (C-ZSM-5 : SiO_2 = 1 : 1 wt/wt) (mesoporous SiO_2 : purchased from Jicang nano technology Co., Ltd., Nanjing, China; this sample shows a high BET specific surface area (745.34 m^2 g^{-1}) consisting of uniform mesopores of 2.5 nm without any microporosity; Si/Al atomic ratio (∞)). That is, the modification of acid sites by inactive silica may be effective to prove it. The catalytic activity of C_2-ZSM-5 sample as a function of time is displayed in Fig. 11A and the average selectivity of the products at steady stage are listed in Table S4 (ESI†). Unfortunately, the C_2-ZSM-5 sample shows worse results than the HA-167-2S-5H zeolite and only slight differences in catalytic activity and selectivity were observed between the C_2-ZSM-5 and C-ZSM-5 samples. Compared to the C-ZSM-5 sample, C_2-ZSM-5 shows lower selectivities for light olefins ($C_2^=$–$C_4^=$ (59.7% vs. 61.4%)), ethylene (9.9% vs. 11.1%) and propylene (31.9% vs. 33.1%), while their selectivities toward C_1–C_4 alkanes (6.1% vs. 5.3%), butylenes (17.9% vs. 17.2%) and C_5^+ hydrocarbons (34.6% vs. 33.3%) are higher (Table S4, ESI†), thus resulting in a higher ratio of propylene/ethylene (P/E = 3.2). On the other hand, the catalytic lifetime of C_2-ZSM-5 did not show any changes compared to that of C-ZSM-5 (6 h vs. 6 h), suggesting that the lowered acid concentration and strength did not slow down the deactivation of the catalysts and the simple dilution of acid sites of C-ZSM-5 with mesoporous SiO_2 had a negligible impact on the catalytic performance. Hence, the above experimental evidence converged to prove that the high value of L acid sites could not be responsible for the rapid deactivation of C-ZSM-5. Taking into account the superior textural properties of mesoporous SiO_2 (very high surface area and uniform mesopores), the cause of the lower activity observed for the C_2-ZSM-5 sample compared to the HA-167-2S-5H catalyst is to be due to its inferior textural properties, i.e. low V_{micro}, poor accessibility of acidic sites and low crystallinity. It is particularly noteworthy that dilution of catalyst with mesoporous SiO_2 can effectively improve the heat conduction in the bed, which ensures the steady processing of MTP reaction.
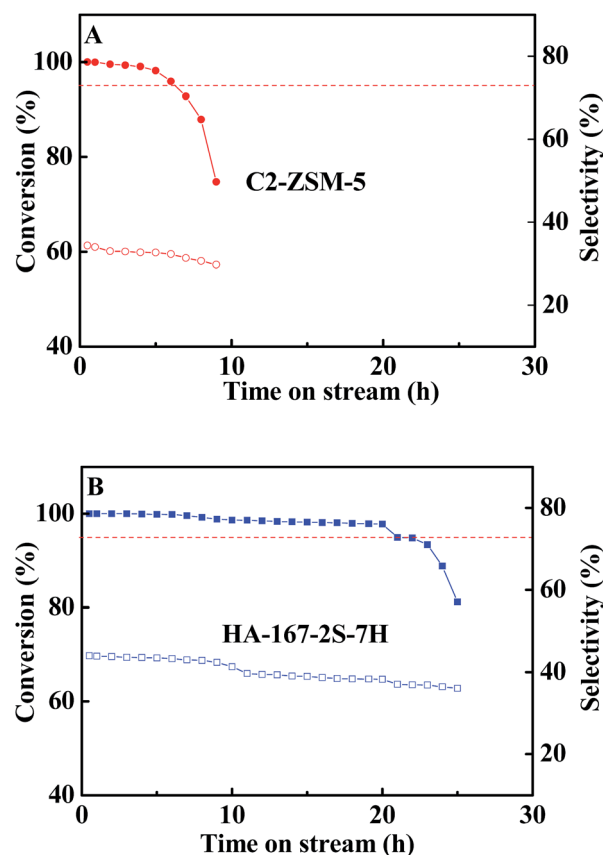

Fig. 11 Conversion of methanol and selectivity of propylene over zeolites C_2-ZSM-5 (A) and HA-167-2S-7H (B). Reaction conditions: WHSV = 12 h^{-1}, T = 470 °C, n(CH$_3$OH) : n(H$_2$O) = 1 : 1, P = 1 bar.

As we all known, the acidity, including the acid intensity is viewed as a vital factor in determining catalytic performance in the MTP reaction.[61] However, in this case, for the C-ZSM-5 sample, the situation is different because it is constituted by bulk zeolite crystals with pure microporosity and amorphous mesoporous particles. As previously noted, the narrow channels of bulk zeolite crystals strongly impose a restriction on the transport of product molecules, leading to an increase of various secondary reactions which may cause relatively easy coke formation and deactivation of catalysts. Based on the experimental results and the above analysis, it is reasonably speculated that the inferior textural properties (the pure microporosity, low S_{BET}, low V_{micro} and low S_{ext}), poor accessibility of acidic sites and low relative crystallinity are the main reasons behind the short lifetime and low target products selectivity of C-ZSM-5, rather than the high value of L acid sites.

The C_1-ZSM-5 catalyst exhibits the shortest lifetime of only 1.5 h and relatively higher olefin ($C_2^=$–$C_4^=$ molecules: 66%) and propylene (38.7%) selectivity compared with C-ZSM-5 catalyst. However, it undergoes rapid coking reactions and shows a sharp deactivation, which can also be explained by its structural properties and acidic properties. In addition to the shortened methanol transfer paths, the formation of C_5^+ was also more or less depressed accordingly (Table S4 (ESI†)).

However, the lowest total acid amount and the highest strong to weak acidity ratio (Table S2 (ESI†)) accelerate deactivation of C_1-ZSM-5 catalyst. In addition, as clearly shown in Table S2 (ESI†), the lowest ratio of B/L and ultra-high L acid amount were also very unfavourable for the catalytic activity of C_1-ZSM-5 catalyst in MTP reaction. As expected, C_1-ZSM-5 holding more strong and less weak acid sites has the shortest lifetime among three samples.

In order to prove the reproducibility of the catalytic performance of the HA-ZSM-5 zeolites, we synthesized and evaluated the HA-167-2S-5H several times and the results indicated that the data in Fig. 10 and Table S4 (ESI†) was reliable. Additionally, the catalytic performance over another HA-ZSM-5 zeolite (HA-167-2S-7H) for MTP reaction was also evaluated under identical conditions. Catalytic activity *versus* time on stream over HA-167-2S-7H sample is displayed in Fig. 11B. As seen, like HA-167-2S-5H, the HA-167-2S-7H also exhibited prominent stability enhancement and its catalytic lifetime (20 h) is nearly 3.3 and 13.3 times longer than that of the C-ZSM-5 (6 h) and C_1-ZSM-5 (1.5 h), respectively.

The average selectivities of the products at steady stage are listed in Table S4 (ESI†). Clearly, in comparison with the C-ZSM-5 and C_1-ZSM-5, the HA-167-2S-7H exhibits the highest selectivities toward light olefins ($C_2^=$–$C_4^=$ (68.5%)), butylenes (22.9%) and propylene (40.3%), while their selectivities toward ethylene (5.3%), C_1–C_4 alkanes (2.9%) and C_5^+ hydrocarbons (28.6%) are lowest (Table S4, ESI†), thus resulting in the highest ratio of propylene/ethylene (P/E = 7.6). The average propylene selectivity of the HA-167-2S-7H sample at steady stage reaches as high as 40.3%, 7.2% and 1.6% higher than that of the C-ZSM-5 and C_1-ZSM-5, respectively.

In addition to the similar desired products distribution, the catalytic lifetime of HA-167-2S-7H was slightly shorter than the HA-167-2S-5H catalyst (20 h *vs.* 22 h), indicating that the addition of an appropriate amount of HTAB to the zeolite synthesis mixture was beneficial to the formation of the well-defined HA-ZSM-5 zeolite with desired structural properties and thus resulting in an enhancement of the catalytic activity and selectivity. Meanwhile, excess HTAB was disadvantageous to the formation of the highly crystalline HA-ZSM-5 zeolite with hierarchical pores and hence caused a slightly decrease in catalytic activity. These results, which are again consistent with the findings from the SEM, XRD and BET analysis.

As mentioned earlier, higher activity and superior selectivity of HA-167-2S-7H should be contributed to by the excellent structural properties, appropriate acidity, suitable strong/weak acid sites ratio, good accessibility of acidic sites and high crystallinity (Tables S1–S4 (ESI†)).

In conclusion, the improved catalytic stability and propylene selectivity of HA-167-2S-7H sample further confirm the reproducibility of the catalytic performance. Meanwhile, these experimental results indicate the necessity of the combination of HTAB and SSC method for the preparation of highly stable MTP catalyst.

Recent studies have proved that catalyst deactivation in the MTP reaction is mainly caused by carbon deposition, for which coke deposition could cover the acid sites or make channels blockage.[64,65] The secondary reactions occurred on the acidic sites are the main reason for carbon deposition on the catalyst surface.[66] Thus, it is necessary to investigate their coking behavior for gaining insight into the dramatic catalytic activity and selectivity improvement by the hierarchical pores design.

Fig. S9 (ESI†) presents the coke deposition on the deactivated C_1-ZSM-5, C-ZSM-5, and HA-167-2S-5H catalysts measured by TG analysis. As can be seen, HA-167-2S-5H contains 2.73 wt% coke deposit after 22 h time on stream, while for C-ZSM-5 and C_1-ZSM-5 the coke deposit are 1.92 wt% and 1.41 wt% after 6 h and 1.5 h, respectively. The average coking rate on HA-167-2S-5H is 0.12% per hour, much lower than that of 0.32% and 0.94% on C-ZSM-5 and C_1-ZSM-5 catalysts. Accordingly, negligible coke deposition and less sensitive to the more coke deposits can be helpful for enhancement of the selectivity of target products (propylene, butylenes and light olefins) and especially catalytic lifetime.

3.6 Formation mechanism of HA-ZSM-5 zeolites

In order to investigate the formation mechanism of HA-ZSM-5 prepared *via* SSC route, the crystallization process was monitored by characterization of samples obtained at different crystallization time of 6, 12, 18, 24, 30 and 36 h. The resultant samples with a molar composition of 100 SiO_2 : 0.6 Al_2O_3 : 7 Na_2O : 1000 H_2O : 5 HTAB : 2 S-1 were systematically characterized by various techniques (including XRD, BET, and SEM).

The XRD patterns of samples prepared at different crystallization times are depicted in Fig. S10 (ESI†), and the relative crystallinity of corresponding samples are listed in Table S5 (ESI†). As shown in Fig. S10 (ESI†), no obvious characteristic peaks of MFI phase are observed after crystallizing for 18 h, indicating the amorphous nature of the obtained samples.

After crystallization for 24 h, a few subtle characteristic peaks related to the MFI phase begin to appear and the relative crystallinity of corresponding sample is merely 61%, which implies the incomplete crystallization of the raw materials. Also, these results illustrate that the primary nucleation induction period is relatively long for the preparation of HA-ZSM-5 zeolites.

The diffraction peak intensity of MFI topology increased rapidly after crystallization for 30 h. This result demonstrates that a rapid crystal growth appeared after the crystallization for 24 h.

The synthesized sample exhibits well-resolved diffraction peaks related to the MFI structure after crystallization for 36 h. In spite of this, the diffraction peaks intensity of MFI topology increased gradually when the crystallization time increased from 30 h to 36 h, which suggest that the HA-ZSM-5 zeolite gradually grows at a relatively slow rate after the crystallization for 30 h.

N_2 adsorption–desorption measurements were performed to observe the variation of the structural properties of samples prepared with different crystallization times. The N_2 adsorption–desorption isotherms and the PSD curves of the samples are depicted in Fig. S11 and S12 (ESI†), respectively. The uptake at $p/p_0 < 0.02$ become more and more apparent with the increase of crystallization time (see Fig. S11 (ESI†)), indicating that the

microporous materials are continuously generated with the increase of crystallization time. In addition, all samples obtained at different crystallization times display a hybrid between type I and type IV isotherms, indicating the existence of inter-crystal mesopores. Additionally, the hysteresis loop grew smaller and it gradually shifted to the low pressure region with the increase of the crystallization time (Fig. S11 (ESI†)). PSD curves (Fig. S12 (ESI†)) also show that mesopore size decreases with increasing crystallization time from 6 h to 36 h. The above results confirmed that the original mesoporous materials are dissolved gradually to form a hierarchical structure.[67,68]

As shown in Table S5 (ESI†), the S_{BET} of the samples increases with the crystallization time increasing; the S_{ext} tends to increase; the V_{micro} of the samples increases gradually, whereas the V_{pore} and V_{meso} decreases. These results are also ascribed to the dissolution of original mesoporous materials and thereby the formation of HA-ZSM-5 zeolite. The variation of structural properties with crystallization time is consistent with the XRD and SEM analyses.

To clarify the structural evolution of the HA-ZSM-5 zeolites, the samples morphology during different periods of crystallization is captured. As displayed in Fig. 12 and inset, small lumps with irregular shape and some seeds could be observed after 6 h crystallization (Fig. 12 (6 h) and inset). As mentioned above, this result may be attributed to the dissolution of the original mesoporous materials and the added S-1 seeds were enwrapped by numerous small sized amorphous materials.

At the crystallization time of 12 h, some irregular aggregates composed of a large number of superfine amorphous nanoparticles with size of about 10 nm and a small amount of subnanocrystals are visible, and the surface of the irregular

aggregates was quite rough, as shown in Fig. 12 (12 h) and inset. In addition, a large number of small holes appear in the external and internal surfaces of the irregular aggregates (see Fig. 12 (12 h)). Meanwhile, the irregular lumps and seeds disappeared completely. These phenomena indicate that the original mesoporous materials are dissolved into the basic unit of ZSM-5 formation. At the same time, the S-1 seeds partly dissolved into a small amount of subnanocrystals with MFI structure.[1]

With the decrease of the irregular aggregates size, more subnanocrystals are formed by consuming the original mesoporous materials after crystallization for 18 h.

As the time is prolonged to 24 h, a large number of subnanocrystals appeared, simultaneously, these subnanocrystals are locally rearranged to form a small amount of superfine nanocrystals. At the same time, the superfine nanocrystals were further aggregated into a small amount of irregular spheres with rough surface (see Fig. 12 (24 h)). Obviously, more and more un-uniform irregular aggregates were obtained by consuming superfine nanocrystals.

After crystallization for 30 h, the sample presents the morphology of sole ellipsoidal aggregates composed of numerous superfine nanocrystals which is similar to that of HA-167-2S-5H. Notably, a small amount of amorphous materials can be observed (Fig. 12 (30 h)).

Further extending the crystallization time to 36 h, the ellipsoidal aggregates size becomes larger and the surface of aggregates becomes rougher (Fig. 12 (36 h)). The HA-ZSM-5 zeolite with high purity and high crystallinity was completely synthesized along with the disappearance of amorphous materials. Therefore, the proper crystallization time is very crucial to the formation of HA-ZSM-5 zeolite.

Based on our previous studies[16,19,30,46,69–72] and the above discussion, the possible formation mechanism of HA-ZSM-5 is proposed in Scheme 1.

As depicted in Scheme 1, the starting step involves the preparation of original mesoporous materials using HTAB as a mesoporous directing agent.

At the beginning of SSC treatment, the original mesoporous materials dissolved gradually into numerous small sized amorphous nanoparticles and reorganized under highly alkaline condition, simultaneously, the S-1 seeds were partially
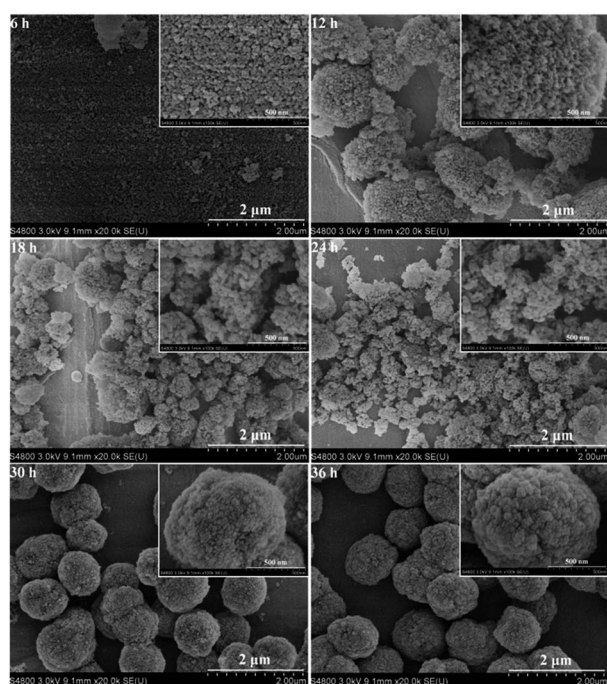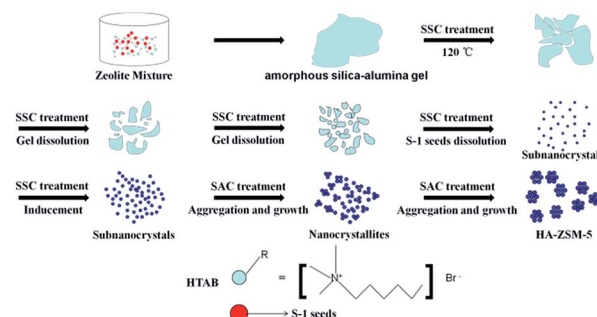

Fig. 12 The SEM images of HA-ZSM-5 samples at different crystallization time.

Scheme 1 Proposed formation process for the synthesis of HA-ZSM-5 zeolites.

dissolved into a handful of subnanocrystals. Some irregular aggregates were formed by a large number of superfine amorphous nanoparticles with size of about 10 nm.

With the induction of the subnanocrystals and the dissolution of the amorphous silica-alumina gel, a large number of subnanocrystals are formed, meanwhile, these subnanocrystals are locally rearranged to form superfine nanocrystals. At this stage, the induction and dissolution of subnanocrystals occur simultaneously.[1] Moreover, HTAB forms small aggregates at relatively lower temperature (120 °C) to stabilize the superfine nanocrystals by reducing the surface Gibbs free energy of nanoparticles.[23] These subnanocrystals interacted with HTAB and the strong coulomb force between them will inhibit the excessive growth of the crystal.

In the following step, numerous superfine nanocrystals aggregated due to their high Gibbs free energy, grow up gradually and finally constantly consume neighboring raw materials to form irregular aggregates in small size.

In the later stages of SSC treatment, a rapid crystal growth of irregular aggregates occurs by the continuous assembly of the superfine nanocrystals. To reach the balance state of minimum energy, the irregular aggregates have experienced 3D expansion to form ellipsoidal aggregates with cauliflower-like morphology in the subsequent crystallization.

Even longer crystallization time led to the growth and aggregation of ellipsoidal aggregates and superfine nanoparticles. As a consequence, all the superfine nanocrystals aggregated to form the abundant intercrystalline mesopores.

Generally, the final crystal size distribution of HA-ZSM-5 samples strongly depend on the number of subnanocrystals formed during the crystallization and on the rate of their formation. These findings are further support previous suggestion that the SSC process follows a kinetics-controlled dissolution/induction/growth/aggregation mechanism.[36]

4. Conclusions

In this work, hierarchical ZSM-5 aggregates (denoted as HA-ZSM-5) zeolites with high crystallinity and abundant intracrystal mesopores have been successfully prepared *via* a solid-like state conversion (SSC) method using the *n*-hexyltrimethylammonium bromide (HTAB) as a mesopore template, which is short crystallization time, operational simplicity and low cost compared with traditional hydrothermal method. Of note is that HTAB can forms small aggregates to stabilize the superfine nanocrystals by lowering their surface Gibbs free energy, and thereby leading to the development of intercrystal mesoporous structure. The large external surface and intracrystal mesopores increase the accessibility of acid sites and improve the diffusion efficiency of large molecules, as a result, the HA-ZSM-5 zeolite exhibits remarkable catalytic activity with a higher propylene selectivity and a longer catalytic life in MTP reaction compared with the C-ZSM-5 and C_1-ZSM-5 samples. Such a facile SSC method produces higher zeolite yield and less wastewater pollution, which has great potential in industrial applications. Furthermore, our work offers a very effective approach to overcome intracrystalline diffusion limitations of

bulky molecules and provides a new perspective on the synthesis of HSZs, where previously only large organic molecules were employed as templates. More importantly, we believe that this approach can also be utilized to design and fabricate other HSZs (such as BETA, FAU, modernite and zeolite X and Y).

Acknowledgements

Notes and references

1 M. Liu, J. Li, W. Jia, M. Qin, Y. Wang, K. Tong, H. Chen and Z. Zhu, *RSC Adv.*, 2015, **5**, 9237–9240.

2 R. Wei, H. Yang and D. Zhang, *RSC Adv.*, 2015, **5**, 63765–63776.

3 G. T. Vuong and T. O. Do, *J. Am. Chem. Soc.*, 2007, **129**, 3810–3811.

4 J. Jiang, Y. Yang, C. Duanmu, Y. Xu, L. Feng, X. Gu and J. Chen, *Microporous Mesoporous Mater.*, 2012, **163**, 11–20.

5 L. Tosheva and V. P. Valtchev, *Chem. Mater.*, 2005, **17**, 2494–2513.

6 Y. Zhang, K. Zhu, X. Zhou and W. Yuan, *New J. Chem.*, 2014, **38**, 5808–5816.

7 A. Boisen, I. Schmidt, A. Carlsson, S. Dahl, M. Brorson and C. J. H. Jacobsen, *Chem. Commun.*, 2003, 958–959.

8 Z. Liu, D. Wu, S. Ren, X. Chen, M. Qiu, G. Liu, G. Zeng and Y. Sun, *RSC Adv.*, 2016, **6**, 15816–15820.

9 A. Janssen, I. Schmidt, C. Jacobsen, A. Koster and K. de Jong, *Microporous Mesoporous Mater.*, 2003, **65**, 59–75.

10 F.-S. Xiao, L. Wang, C. Yin, K. Lin, Y. Di, J. Li, R. Xu, D. S. Su, R. Schlögl, T. Yokoi and T. Tatsumi, *Angew. Chem.*, 2006, **118**, 3162–3165.

11 D. P. Serrano, J. M. Escola and P. Pizarro, *Chem. Soc. Rev.*, 2013, **42**, 4004–4035.

12 Y. Jiang, Y. Wang, W. Zhao, J. Huang, Y. Zhao, G. Yang, Y. Lei and R. Chu, *J. Taiwan Inst. Chem. Eng.*, 2016, **61**, 234–240.

13 X. Wei and P. G. Smirniotis, *Microporous Mesoporous Mater.*, 2006, **89**, 170–178.

14 H. Zhang, Y. Ma, K. Song, Y. Zhang and Y. Tang, *J. Catal.*, 2013, **302**, 115–125.

15 T. Xue, L. Chen, Y. M. Wang and M.-Y. He, *Microporous Mesoporous Mater.*, 2012, **156**, 97–105.

16 F. Meng, Y. Wang, S. Wang, X. Wang and S. Wang, *C. R. Chim.*, 2016, 1–10.

17 M. Choi, K. Na, J. Kim, Y. Sakamoto, O. Terasaki and R. Ryoo, *Nature*, 2009, **461**, 246–249.

18 M. Zhou, A. A. Rownaghi and J. Hedlund, *RSC Adv.*, 2013, **3**, 15596–15599.

19 H. Chen, Y. Wang, F. Meng, H. Li, S. Wang, C. Sun, S. Wang and X. Wang, *RSC Adv.*, 2016, **6**, 76642–76651.

20 K. Egeblad, C. H. Christensen, M. Kustova and C. H. Christensen, *Chem. Mater.*, 2007, **20**, 946–960.

21 K. Na, M. Choi, W. Park, Y. Sakamoto, O. Terasaki and R. Ryoo, *J. Am. Chem. Soc.*, 2010, **132**, 4169–4177.

22 T. Ge, Z. Hua, X. He, Y. Zhu, W. Ren, L. Chen, L. Zhang, H. Chen, C. Lin, H. Yao and J. Shi, *Chin. J. Catal.*, 2015, **36**, 866–873.

23 P. Bai, P. Wu, W. Xing, D. Liu, L. Zhao, Y. Wang, B. Xu, Z. Yan and X. S. Zhao, *J. Mater. Chem. A*, 2015, **3**, 18586–18597.

24 F. Pan, X. Lu, Q. Zhu, Z. Zhang, Y. Yan, T. Wang and S. Chen, *J. Mater. Chem. A*, 2014, **2**, 20667–20675.

25 S. Inagaki, K. Nakatsuyama, Y. Saka, E. Kikuchi, S. Kohara and M. Matsukata, *J. Phys. Chem. C*, 2007, **111**, 10285–10293.

26 X. He, T. Ge, Z. Hua, J. Zhou, J. Lv, J. Zhou, Z. Liu and J. Shi, *ACS Appl. Mater. Interfaces*, 2016, **8**, 7118–7124.

27 Y. Zhang, K. Zhu, X. Zhou and W. Yuan, *New J. Chem.*, 2014, **38**, 5808–5816.

28 Z. Deng, Y. Zhang, J. Zheng, K. Zhu and X. Zhou, *New J. Chem.*, 2015, **39**, 7777–7780.

29 R. Cai, Y. Liu, S. Gu and Y. Yan, *J. Am. Chem. Soc.*, 2010, **132**, 12776–12777.

30 H. Li, Y. Wang, F. Meng, H. Chen, C. Sun and S. Wang, *RSC Adv.*, 2016, **6**, 99129–99138.

31 L. Ren, Q. Wu, C. Yang, L. Zhu, C. Li, P. Zhang, H. Zhang, X. Meng and F.-S. Xiao, *J. Am. Chem. Soc.*, 2012, **134**, 15173–15176.

32 H. Li, Y. Wang, F. Meng, H. Chen, C. Sun and S. Wang, *RSC Adv.*, 2016, **6**, 99129–99138.

33 T. Zhang, Y. Wang, S. Wang, X. Wu, P. Yao, W. Feng, Y. Lin and J. Xu, *React. Kinet., Mech. Catal.*, 2015, **114**, 735–752.

34 H. Xiao, J. Zhang, X. Wang, Q. Zhang, H. Xie, Y. Han and Y. Tan, *Catal. Sci. Technol.*, 2015, **5**, 4081–4090.

35 Z. Wan, W. Wu, W. Chen, H. Yang and D. Zhang, *Ind. Eng. Chem. Res.*, 2014, **53**, 19471–19478.

36 C. A. Emeis, *J. Catal.*, 1993, **141**, 347–354.

37 T. Ge, Z. Hua, X. He, J. Lv, H. Chen, L. Zhang, H. Yao, Z. Liu, C. Lin and J. Shi, *Chem.–Eur. J.*, 2016, **22**, 7895–7905.

38 S. Narayanan, J. J. Vijaya, S. Sivasanker, S. Yang and L. J. Kennedy, *Chin. J. Catal.*, 2014, **35**, 1892–1899.

39 Y. Gao, G. Wu, F. Ma, C. Liu, F. Jiang, Y. Wang and A. Wang, *Microporous Mesoporous Mater.*, 2016, **226**, 251–259.

40 C. S. Cundy and P. A. Cox, *Microporous Mesoporous Mater.*, 2005, **82**, 1–78.

41 V. P. Valtchev and K. N. Bozhilov, *J. Am. Chem. Soc.*, 2005, **127**, 16171–16177.

42 Q. Yu, Q. Zhang, J. Liu, C. Li and Q. Cui, *CrystEngComm*, 2013, **15**, 7680–7687.

43 B. K. Singh, D. Xu, L. Han, J. Ding, Y. Wang and S. Che, *Chem. Mater.*, 2014, **26**, 7183–7188.

44 Y. Wang, R. Wang, D. Xu, C. Sun, L. Ni, W. Fu, S. Zeng, S. Jiang, Z. Zhang and S. Qiu, *New J. Chem.*, 2016, **40**, 4398–4405.

45 J. C. Groen, L. A. A. Peffer, J. A. Moulijn and J. Pérez-Ramírez, *Chem.–Eur. J.*, 2005, **11**, 4983–4994.

46 H. Chen, Y. Wang, F. Meng, C. Sun, H. Li, Z. Wang, F. Gao, X. Wang and S. Wang, *Microporous Mesoporous Mater.*, 2017, **109**, 1–9.

47 P. L. Llewellyn, J. P. Coulomb, Y. Grillet, J. Patarin, G. Andre and J. Rouquerol, *Langmuir*, 1993, **9**, 1852–1856.

48 J. C. Groen and J. Pérez-Ramírez, *Appl. Catal., A*, 2004, **268**, 121–125.

49 D. P. Gamliel, H. J. Cho, W. Fan and J. A. Valla, *Appl. Catal., A*, 2016, **522**, 109–119.

50 Q. Wang, Y. Wei, S. Xu, M. Zhang, S. Meng, D. Fan, Y. Qi, J. Li, Z. Yu, C. Yuan, Y. He, S. Xu, J. Chen, J. Wang, B. Su and Z. Liu, *Chin. J. Catal.*, 2014, **35**, 1727–1739.

51 J. Zhao, Z. Hua, Z. Liu, Y. Li, L. Guo, W. Bu, X. Cui, M. Ruan, H. Chen and J. Shi, *Chem. Commun.*, 2009, 7578–7580.

52 P. Marturano, L. Drozdova, A. Kogelbauer and R. Prins, *J. Catal.*, 2000, **192**, 236–247.

53 J. Ahmadpour and M. Taghizadeh, *C. R. Chim.*, 2015, **18**, 834–847.

54 M. Milina, S. Mitchell, P. Crivelli, D. Cooke and J. Pérez-Ramírez, *Nat. Commun.*, 2014, **5**, 3922.

55 M. Milina, S. Mitchell, D. Cooke, P. Crivelli and J. Pérez-Ramírez, *Angew. Chem., Int. Ed.*, 2014, **54**, 1591–1594.

56 J. Ahmadpour and M. Taghizadeh, *J. Nat. Gas Sci. Eng.*, 2015, **23**, 184–194.

57 J. Kim, M. Choi and R. Ryoo, *J. Catal.*, 2010, **269**, 219–228.

58 F. Yaripour, Z. Shariatinia, S. Sahebdelfar and A. Irandoukht, *Microporous Mesoporous Mater.*, 2015, **203**, 41–53.

59 Y. Yang, C. Sun, J. Du, Y. Yue, W. Hua, C. Zhang, W. Shen and H. Xu, *Catal. Commun.*, 2012, **24**, 44–47.

60 M. Rostamizadeh and A. Taeb, *J. Ind. Eng. Chem.*, 2015, **27**, 297–306.

61 S. Zhang, Y. Gong, L. Zhang, Y. Liu, T. Dou, J. Xu and F. Deng, *Fuel Process. Technol.*, 2015, **129**, 130–138.

62 W. Kim and R. Ryoo, *Catal. Lett.*, 2014, **144**, 1164–1169.

63 Z. Wan, W. Wu, W. Chen, H. Yang and D. Zhang, *Ind. Eng. Chem. Res.*, 2014, **53**, 19471–19478.

64 F. Schmidt, C. Hoffmann, F. Giordanino, S. Bordiga, P. Simon, W. Carrillo-Cabrera and S. Kaskel, *J. Catal.*, 2013, **307**, 238–245.

65 M. Stöcker, *Microporous Mesoporous Mater.*, 1999, **29**, 3–48.

66 F. Yaripour, Z. Shariatinia, S. Sahebdelfar and A. Irandoukht, *Microporous Mesoporous Mater.*, 2015, **203**, 41–53.

67 M. Li, I. Nartey Oduro, Y. Zhou, Y. Huang and Y. Fang, *Microporous Mesoporous Mater.*, 2016, **221**, 108–116.

68 M. Choi, H. S. Cho, R. Srivastava, C. Venkatesan, D.-H. Choi and R. Ryoo, *Nat. Mater.*, 2006, **5**, 718–723.

69 F. Meng, Y. Wang and S. Wang, *RSC Adv.*, 2016, **6**, 58586–58593.

70 F. Meng, Y. Wang, S. Wang and S. Wang, *React. Kinet., Mech. Catal.*, 2016, **119**, 671–683.

71 Y. Wang, S. Wang, F. Meng, S. Wang, J. Ye and Y. Lin, *Trans. Tianjin Univ.*, 2017, **23**, 43–50.

72 X. Wang, H. Chen, F. Meng, F. Gao, C. Sun, L. Sun, S. Wang, L. Wang and Y. Wang, *Microporous Mesoporous Mater.*, 2017, **243**, 271–280.